Optimizing against Infeasible Inclusions from Data for Semantic Segmentation through Morphology

Shamik Basu¹, Luc Van Gool^{1,3}, and Christos Sakaridis¹

²ETH Zürich
¹University Of Bologna
³INSAIT, Sofia University St. Kliment Ohridski

Abstract

State-of-the-art semantic segmentation models are typically optimized in a data-driven fashion, minimizing solely perpixel or per-segment classification objectives on their training data. This purely data-driven paradigm often leads to absurd segmentations, especially when the domain of input images is shifted from the one encountered during training. For instance, state-of-the-art models may assign the label "road" to a segment that is included by another segment that is respectively labeled as "sky". However, the ground truth of the existing dataset at hand dictates that such inclusion is not feasible. Our method, Infeasible Semantic Inclusions (InSeIn), first extracts explicit inclusion constraints that govern spatial class relations from the semantic segmentation training set at hand in an offline, data-driven fashion, and then enforces a morphological yet differentiable loss that penalizes violations of these constraints during training to promote prediction feasibility. InSeIn is a light-weight plug-and-play method, constitutes a novel step towards minimizing infeasible semantic inclusions in the predictions of learned segmentation models, and yields consistent and significant performance improvements over diverse state-of-the-art networks across the ADE20K, Cityscapes, and ACDC datasets. https: //github.com/SHAMIK-97/InSeIn/tree/main

1. Introduction

Semantic segmentation is a fundamental task in computer vision and enables many downstream applications. The last decade has witnessed dramatic advances in this dense prediction task, driven by the introduction of end-to-end learned network architectures for solving it [5–7, 9, 20, 30, 34, 41, 47, 48, 50] and the development of ever stronger backbones coming from image classification [14, 21, 29, 37,

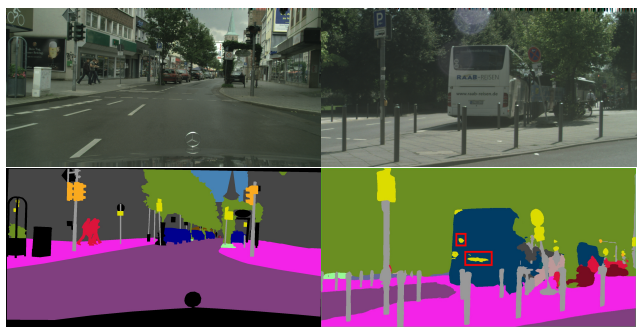


Figure 1. Left: A *traffic light* segment includes a *building* segment in a semantic annotation from the ground truth of the dataset, which is a feasible inclusion. Right: A *bus* segment includes *traffic sign* segments (in the red boxes) in a semantic prediction, which is an **infeasible inclusion**. Our method addresses such physical infeasibilities in semantic segmentation. Best viewed on a screen and zoomed in.

42, 49]. Indeed, designing a suitable backbone for dense semantic prediction that balances global context aggregation with preservation of fine local details has been a primary research direction in semantic segmentation. However, merely optimizing the backbone architecture neglects the structured prediction character of the problem. In particular, the simple optimization of cross-entropy loss terms even by state-of-the-art network architectures [9, 41] essentially poses semantic segmentation as a set of independent pixel-level or- at best-segment-level prediction problems and only loosely promotes *regularity* of the complete image-level outputs via the shared computation in the network across neighboring pixels. Very few deep-learningbased works [26] have focused on designing objectives that originate from the interaction between different pixels in the output predictions, and those that do focus only on local neighborhoods rather than large image regions. To the best of our knowledge, no previous method in semantic segmentation with deep learning has considered high-level pairwise objectives at the coarse level of semantic segments.

Aiming at promoting conformity of semantic segmentation models to high-level constraints, yet adhering to the taxonomy of the dataset at hand, we present a new method named Infeasible Semantic Inclusions (InSeIn). Our method has been empirically motivated by the observation that various state-of-the-art semantic segmentation networks [1, 9, 44, 48] make errors in their predictions, which are misclassifications or false positives, as illustrated in Fig. 1. In particular, based on the Cityscapes [11] taxonomy, a road segment cannot be entirely included in/surrounded by a sky segment, and the same holds for traffic sign and bus respectively. We term such segment inclusions infeasible inclusions and use them as an exemplary type of constraint that can provide a segmentation model with higher-level conformity based on the feasible spatial configurations of semantic segments in the ground truth.

While it is possible to exhaustively consider all pairs of semantic classes in the dataset at hand and manually determine which of them correspond to such infeasible inclusions, we argue and experimentally evidence that infeasible inclusions can be directly identified from large-scale data. More specifically, InSeIn first processes the training set offline before training in a single pass and automatically identifies all class pairs for which a segment of the one class includes a segment of the other at least once in the data. InSeIn prunes this inclusion pair set by thresholding the relative frequency of each inclusion with respect to the cooccurrence of the respective pair to limit the impact of potential noise in the labels. The pairs obtained after pruning are valid inclusion pairs (cf. Fig. 1-left), and InSeIn should and does not penalize such inclusions in the outputs of the segmentation network. By contrast, pairs of co-occurring classes for which a complete inclusion of one class by the other is never found in the large-scale data are deemed as infeasible inclusion pairs, and they contribute to a feasibility objective that we define for optimization during training.

More specifically, the major contribution of InSeIn is a novel inclusion loss, which is used as an additional objective besides standard cross-entropy for optimizing a generic segmentation network. Our inclusion loss is computed based on the softmax outputs of the employed network, similarly to cross-entropy, which allows its general application to the vast majority of deep-learning-based semantic segmentation models. The key idea of computing this loss is to identify "soft" infeasible inclusions, which occur as regions in the softmax score maps of infeasible inclusion class pairs in which the ranking of the two softmax values is inverted compared to their surroundings. We recognize that this simply amounts to a grayscale morphological area opening [16] and derive a differentiable, parameter-free, and efficient implementation of it, which is normally included in the forward and backward pass of standard backpropagation.

We have achieved a consistent performance improvement with InSeIn across three central semantic segmentation benchmarks, i.e. ADE20K [52], Cityscapes [11], and ACDC [36], and across a variety of state-of-the-art semantic segmentation networks on which we have implemented our method, i.e. SegFormer [44], OCRNet [48], Mask2Former [9], OneFormer [25] and SegMAN [15]. Importantly, we have observed a substantial quantitative reduction of infeasible inclusions in our semantic predictions.

2. Related Work

Semantic segmentation deals **Semantic Segmentation.** with pixel classification. Pre-deep learning era methods mainly used lines and contour detection to classify similar pixel groups. Pixel misclassifications are mainly associated with boundary regions of any class segment and are studied in [31]. Here they classified pixel errors into 3 categories: false positives where the predicted edges erroneously appear in non-boundary areas, merging error occurs when the predicted results fail to capture the corresponding edges, resulting in false negatives and displacement error arises when the predicted edges deviate from their true positions. Such displacements may occur when the image features are misaligned. Pre-deep learning era attempted to segment misclassified pixels using graph searching, Laplace operator and other heuristic methods [17, 18, 32, 35, 39, 45].

Modern semantic segmentation methods. The challenge to classify pixels in semantic segmentation is studied in [27] where the authors designed an architecture comprised of several sub-models arranged in a layer cascade fashion. Another paper [12, 43, 46] where the authors devised a framework for nighttime segmentation, where the input data is highly noisy. In this work, they have designed a seperate module to segment hard regions in an image and another module to segment the easy regions. Finally they merged the output of 2 modules to get the final prediction. Another paper [13] where authors divided the input image into several patches and visualized the whole image as a unidirectional acyclic graph where the vertices are patches. Then they constituted a sperate ground truth which constitutes a seperate class for the boundaries and optimzed the model with the newly formed ground truth.

Contribution of loss function in Semantic segmentation. Pixel misclassification problem in segmentation task is handled using depth cues in semantic segmentation in the paper [19, 33]. Here the authors constituted 2 loss-weight modules which output a loss weight map by employing two depth-related measurements of hard pixels: Depth Prediction Error and Depth-aware Segmentation Error. The loss weight map is optimized with segmentation loss to train the network. Another paper [4] devised a custom loss function to tackle misclassification by leveraging the sigmoid function to increase the loss and loss derivative of misclassified

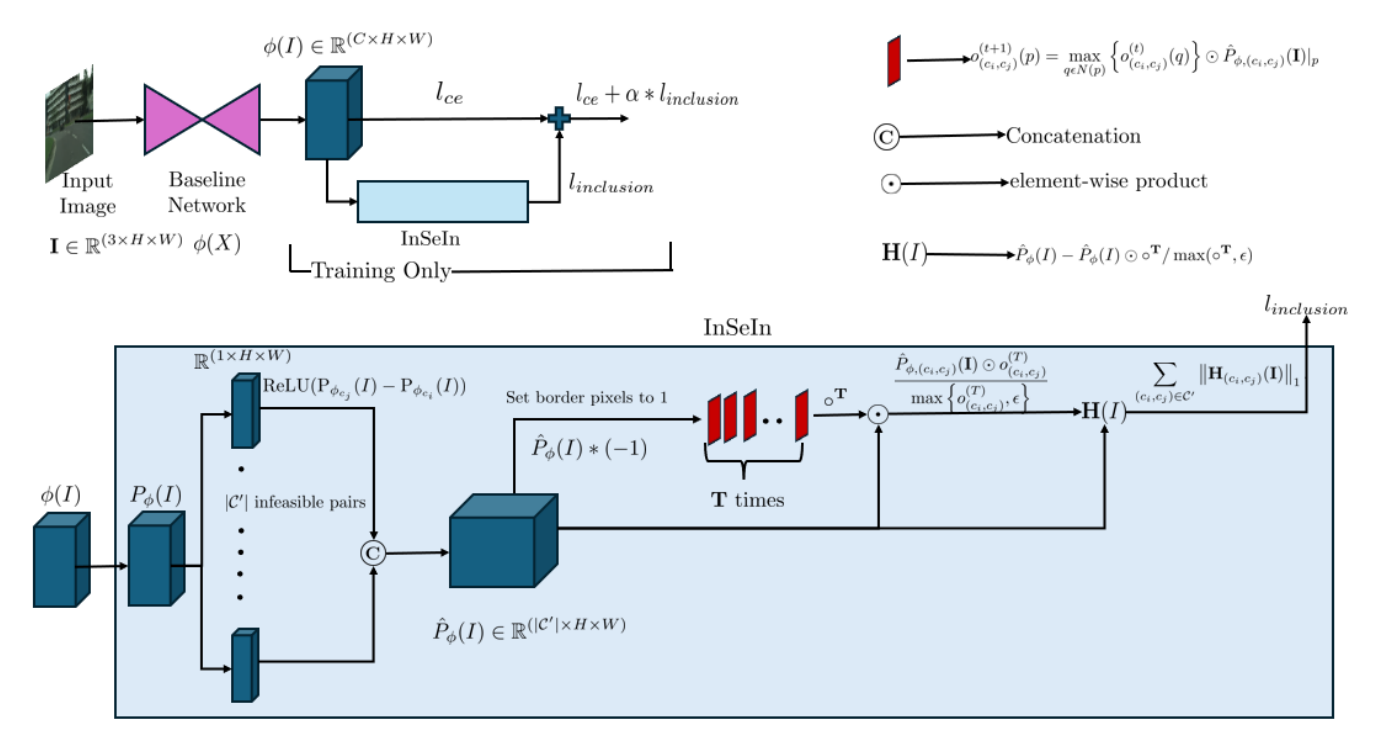


Figure 2. **Overview of InSeIn.** Top left: the complete network architecture, where the standard cross-entropy loss $l_{\rm ce}$ from the baseline network ϕ is added to the inclusion loss $l_{\rm inclusion}$ computed by InSeIn. Bottom: The pipeline of InSeIn. For the softmax outputs $P_{\phi}(I)$ of the network and for each pair of classes $(c_i, c_j) \in \mathcal{C}'$ that signifies an infeasible inclusion where c_i cannot include c_j , we take the difference of the respective softmax scores, $P_{\phi c_j}(I) - P_{\phi c_i}(I)$, and rectify it with a ReLU. After concatenating all such \mathcal{C}' rectified difference maps channel-wise into $\hat{P}_{\phi}(I)$, we negate the latter and set its border pixels to 1. After that, an iterative operation for area opening is performed T times on $\hat{P}_{\phi}(I)$. In each iteration, we perform max-pooling with a 3x3 kernel and a stride of 1, and the result is multiplied with $\hat{P}_{\phi}(I)$ element-wise. The final area-opened tensor channels differ from their counterparts in $\hat{P}_{\phi}(I)$ only across regions of incorrect inclusions. This element-wise difference is stored in $\mathbf{H}(I)$ and the L_1 norm of the latter, capturing both the spatial extent and the intensity of infeasible inclusions, constitutes the inclusion loss $l_{\rm inclusion}$ employed in InSeIn.

and uncertain pixels. Another popular method is Binary Focal Loss [2, 23, 24, 28, 40] where the author used the normal cross entropy loss and down-weighted the easily classified pixels. Another paper [38] developed a region wise(RW) loss through pixel-wise multiplication of RW map and softmax output for biomedical image segmentation.

All the above methods attempted to solve false positive regions at the pixel level. None of them takes into account the pairwise semantic relationship between the classes, as we do in our approach. We have also observed that false positives occur not only at the hard regions but also in easy-to-classify segments. We focus on the case of false positive segments in the form of infeasible inclusions and aim at optimizing against this type of error.

3. InSeIn

3.1. Method Overview

Fig. 2 shows the architectural overview of InSeIn. A 2D semantic segmentation network $\phi(X)$ is fed with an image $\mathbf{I} \in \mathbb{R}^{3 \times H \times W}$ and produces the initial output $\phi(\mathbf{I}) \in$

 $\mathbb{R}^{C imes H imes W}$, where C is the number of classes. InSeIn takes $\phi(\mathbf{I})$ as input and computes a novel inclusion loss, $l_{\text{inclusion}}$. We identify infeasible inclusions for class pairs of interest via a morphological area opening operation, which is fully differentiable and is normally included in the forward and backward pass during training. Our loss $l_{\text{inclusion}}$ is then added to the standard cross-entropy loss l_{ce} for $\phi(\mathbf{I})$ to obtain the total loss as

$$l_{\text{total}} = l_{\text{ce}} + \alpha l_{\text{inclusion}}, 0 < \alpha < 1.$$
 (1)

 $l_{\rm total}$ is normally backpropagated to optimize the weights of ϕ . Thus, InSeIn is a differentiable morphological module that enhances the optimization and conformity of any segmentation network by integrating high-level data-driven constraints in the form of infeasible inclusions. Notably, the InSeIn module is both learned parameter-free *and* differentiable, allowing gradients to propagate through the network during training. The only extra parameter of InSeIn is α in (1), a hyperparameter which is used to balance the inclusion loss and the standard cross-entropy loss.

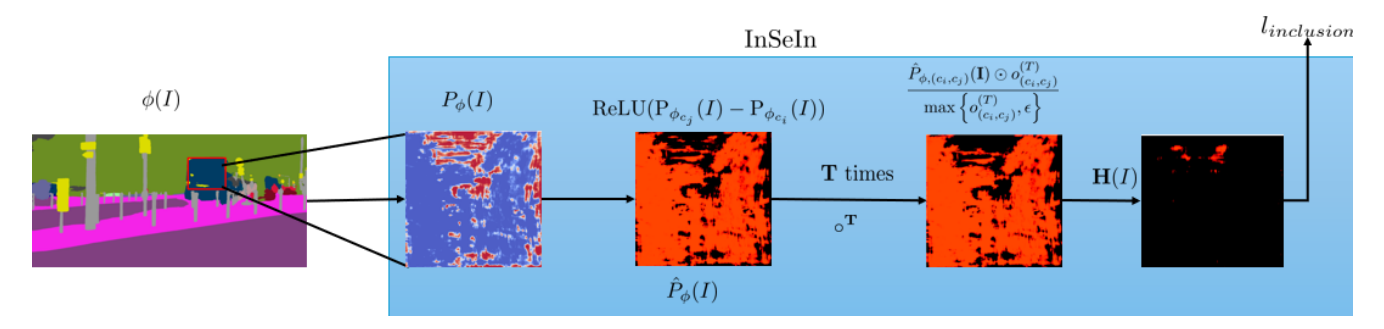


Figure 3. Visualization of feature maps within InSeIn for a class pair corresponding to an infeasible inclusion. In this example semantic prediction of SegFormer [44] on Cityscapes [11], bus infeasibly includes traffic sign. In the blue frame, we first show the difference map between the softmax scores of the two classes using the coolwarm colormap, where blue tones indicate larger scores for traffic sign and red for bus, respectively. We rectify the difference between the two softmax maps and show only the respective channel of the 3D tensor $\hat{P}_{\phi}(I)$, where black indicates zeros and red tones indicate positive values. The area opening operation is performed on $\hat{P}_{\phi}(I)$ and the regions in which $\hat{P}_{\phi}(I)$ is positive (red) but which are not connected to the border, i.e. traffic sign segments infeasibly included in bus segments, are opened. Exactly these segments are isolated in the final tensor $\mathbf{H}(\mathbf{I})$ and are used to compute our inclusion loss $l_{\text{inclusion}}$.

3.2. Computing Infeasible Inclusion Pairs

We apply Algorithm 1 to the training split of the dataset at hand for optimizing and evaluating the segmentation model, to compute the set $\mathcal U$ of class pairs corresponding to feasible, or valid, inclusions. Intuitively, $\mathcal U$ contains class pairs for which a segment of the first class includes a segment of the second one at least in one case in the training set. The set of class pairs corresponding to *infeasible inclusions*, $\mathcal C'$, is then simply the set-theoretic difference $\mathcal C'=\mathcal P\setminus\mathcal U$, where $\mathcal P$ is the set of all possible non-identical class pairs. In particular, any pair in $\mathcal U$ whose relative frequency of inclusion with respect to co-occurance of the class pairs is less than 2% is considered noise or an outlier, and is removed from $\mathcal U$.

In Algorithm 1, we first compute for each annotation S in the training set two binary masks of the same dimension as S, in which pixels labeled as class p and class q are set as foreground, respectively. We then compute the connected components of class q, i.e. the class whose possibility to be included is checked, in mask_2. For each such connected component, we fill any holes inside it to remove any interior contour in the next step, as it is irrelevant. After that, we compute the outer contour of the connected component at hand based on an 8-neighborhood and check whether it fully falls into pixels belonging to class p. If the latter is true and the length of the contour is non-negligible, we declare the case at hand as a valid inclusion, and then if the relative frequency of the inclusion to the co-occurrence of the pair is non-negligible, we add the pair (p,q) to the set \mathcal{U} .

3.3. Inclusion Loss

To compute our novel inclusion loss, we operate on the softmax maps $P_{\phi}(\mathbf{I})$ output by the segmentation network and index them channel-wise for each of the $|\mathcal{C}'|$ infeasible inclusion pairs. Our core intuition is to identify in the pairs of softmax score maps that correspond to each infeasible inclusion case in \mathcal{C}' those regions across which class c_j —the includee—has a larger score than class c_i —the includer—and around which the opposite is true. These regions indicate "soft" infeasible inclusions in the softmax predictions, which should be penalized proportionally to the area they occupy and to the variable "intensity" of the inclusion, i.e. the magnitude of the difference between the softmax scores of classes c_i and c_j at each pixel of these regions. The computation of such a loss, which we term the inclusion loss, can be directly achieved in a differentiable formulation, amenable to standard backpropagation, via a grayscale morphological area opening of the aforementioned softmax difference maps. We implement this opening through an iterative algorithm, detailed in the following.

For each "infeasible pair" $(c_i,c_j)\in\mathcal{C}'$, we denote with $\mathrm{P}_{\phi_{c_i},c_j}(\mathbf{I})\in\mathbb{R}^{2 imes H imes W}$ the concatenation of $\mathrm{P}_{\phi_{c_i}}(\mathbf{I})$ and $\mathrm{P}_{\phi_{c_j}}(\mathbf{I})$. The difference between the two channels of the latter tensor is rectified with a ReLU as $\mathrm{ReLU}(\mathrm{P}_{\phi_{c_j}}(\mathbf{I})-\mathrm{P}_{\phi_{c_i}}(\mathbf{I}))\in\mathbb{R}^{1 imes H imes W}$ (cf. Fig. 2). After that, all $|\mathcal{C}'|$ rectified pairwise differences are concatenated to obtain the tensor $\hat{P}_{\phi}(\mathbf{I})\in\mathbb{R}^{|\mathcal{C}'| imes H imes W}$.

For each $(c_i,c_j)\in\mathcal{C}'$, we initialize a running map $o_{(c_i,c_j)}^{(0)}\in\mathbb{R}^{1\times H\times W}$ so that its border pixels are set to 1 and the rest are equal to 0. The intuition here is that infeasibly included regions are always disconnected from the border of the image. Thus, positive values of the map $o_{(c_i,c_j)}^{(t)}$ that are gradually propagated from the border to the interior of the image via iterative 8-neighborhood-based dilation (a.k.a. max-pooling) will *never* reach the aforementioned regions if at each iteration they are multiplied with $\mathrm{ReLU}(\mathrm{P}_{\phi_{c_j}}(\mathbf{I})-\mathrm{P}_{\phi_{c_i}}(\mathbf{I}))$, as the latter is 0 everywhere around infeasibly included regions. The above, intuitively described iterative operation can be formally written as

Algorithm 1 Computing the set $\mathcal U$ of feasible inclusion class pairs from the training set ground-truth annotations $\mathcal S$. The set $\mathcal P$ contains all pairs of non-identical class labels for the dataset taxonomy. We aim to check whether the first element of the pair, p, can include the second one, q. We are taking 5 pixels as the minimum threshold for a contour of q completely overlapping with any segment of p. Function $\mathbf C$ returns (i) the number of connected segments of class q in the input annotation, and (ii) a discrete image, with each pixel labeled with its connected component ID or 0 for the background. Function $\mathbf F$ fills the holes of the mask of the connected component at hand. Then, function $\mathbf C$ ont returns a binary image in which only pixels belonging to the outer contour of the respective connected component are set.

```
Require: \mathcal{P} = \{(p,q) : p \in \{1,\ldots,C\}, q \in \{1,\ldots,C\} \setminus \{1,\ldots,C\} \}
Require: S = \{I : I \in \mathbb{N}^{1,H,W}\}
Ensure: Set \mathcal{U} of feasible inclusion class pairs
  1: count = 0
  2: count\_freq = 0
  3: \mathcal{U} \leftarrow \emptyset
  4: for (p,q) \leftarrow \mathcal{P} do
           for S \leftarrow \mathcal{S} do
                \begin{aligned} & \texttt{mask\_1} \leftarrow \mathbb{1}[S = p] \in \mathbb{R}^{1 \times H \times W} \\ & \texttt{mask\_2} \leftarrow \mathbb{1}[S = q] \in \mathbb{R}^{1 \times H \times W} \end{aligned}
  6:
  7:
                if mask_1 not empty ∧ mask_2 not empty
  8:
      then
  9:
                     count\_freq \leftarrow count\_freq + 1
 10:
                component, noOFLabels \leftarrow \mathbf{C}(\text{mask\_2})
 11:
                for l \leftarrow 1 to noOFLabels do
 12:
                     comp_mask \leftarrow (1[component = l])
 13:
                     comp\_filled \leftarrow \mathbf{F}(comp\_mask)
 14:
                     contour ← Cont(comp_filled)
 15:
                     result \leftarrow contour \land mask_1
 16:
                     if NNZ(result) = NNZ(contour) \land
 17:
      NNZ(contour) > 5 then
 18:
                          count \leftarrow count + 1
 19:
                          break
                     end if
20:
                end for
21:
22:
           if count/count_freq *100 > 2 then
23:
                \mathcal{U} \leftarrow \mathcal{U} \cup \{(p,q)\}
24:
                count = 0
25:
                count\_freq = 0
26:
27:
           end if
28: end for
```

$$o_{(c_i,c_j)}^{(t+1)}(p) = \max_{q \in N(p)} \left\{ o_{(c_i,c_j)}^{(t)}(q) \right\} \odot \hat{P}_{\phi,(c_i,c_j)}(\mathbf{I})|_p, \quad (2)$$

where N(p) denotes the structuring element of the dilation

operator or, equivalently, the max-pooling kernel, which we set to an 8-connected neighborhood, i.e. a 3x3 kernel. We iterate (2) T times, where $T = \max\{2, \min\{H, W\}/2\}$ and H and W are the height and width of the input image I. Namely, we iterate for the minimal number of times that is required for initial positive values at image borders in $o_{(c_i,c_j)}^{(0)}$ to be able to reach any pixel in the interior. The final map $o_{(c_i,c_j)}^{(T)}$ is by construction 0 at all pixels that belong to infeasibly included regions. This property implies that

$$\frac{\hat{P}_{\phi,(c_i,c_j)}(\mathbf{I}) \odot o_{(c_i,c_j)}^{(T)}}{\max\left\{o_{(c_i,c_j)}^{(T)},\epsilon\right\}}$$
(3)

constitutes the grayscale area opening we are after for the infeasible inclusion class pair (c_i, c_j) (cf. Fig. 3), where ϵ is a small positive constant.

The relevant quantity for computing our inclusion loss is the difference between the original rectification output and its area opening from (3). This difference is given by

$$\mathbf{H}_{(c_i,c_j)}(\mathbf{I}) = \hat{P}_{\phi,(c_i,c_j)}(\mathbf{I}) - \frac{\hat{P}_{\phi,(c_i,c_j)}(\mathbf{I}) \odot o_{(c_i,c_j)}^{(T)}}{\max \left\{ o_{(c_i,c_j)}^{(T)}, \epsilon \right\}}.$$
(4)

We perform the above computations for all $(c_i, c_j) \in \mathcal{C}'$. Finally, our inclusion loss is computed as the sum of the L_1 norms of tensors \mathbf{H} across all $(c_i, c_j) \in \mathcal{C}'$ via

$$l_{\text{inclusion}} = \sum_{(c_i, c_j) \in \mathcal{C}'} \left\| \mathbf{H}_{(c_i, c_j)}(\mathbf{I}) \right\|_1.$$
 (5)

4. Experiments

4.1. Datasets

Cityscapes. Cityscapes [11] is a driving dataset. The dataset has 19 classes and includes 2975 training, 500 validation, and 1525 test images with fine annotations and 20000 additional coarsely annotated training images.

ADE20K. We have used the dataset ADE20K [52]. There are 150 classes and diverse scenes with 1038 image-level labels. The dataset is divided into 20K, 2K, and 3K images for training, validation, and testing, respectively.

ACDC. The ACDC dataset [36] consists of driving scenes under adverse conditions such as fog, night, rain, and snow. It has the same 19 classes as Cityscapes. The dataset is divided into 1600 training, 406 validation, and 2000 test images.

4.2. Implementation Details

The softmax maps $P_{\phi}(\mathbf{I})$ input to InSeIn are first resized to $C \times 256 \times 256$. The kernel size of the max-pooling used is 3×3 with a stride of 1 and a padding of 1 to preserve spatial dimensions and to check for any connected components not sharing the border pixels. Random sampling on $|\mathcal{C}'|$ is

Table 1. Comparison with state-of-the-art semantic segmentation methods on ADE20K, Cityscapes and ACDC. *: multiscale testing. Results are reported on the Cityscapes test set, the ADE20K validation set, and the ACDC test set.

Method	Backbone	ADE20K	Cityscapes	ACDC
PSPNet [50]	ResNet50	44.4	78.5	-
DeepLabv2 [6]	ResNet-101	-	71.4	55.3
DeepLabv3+ [8]	ResNet-101	44.1	80.9	70.0
HRNet [41]	ResNet	43.1	80.9	75.0
OCRNet [48]	HRNetV2-W48	45.6*	82.4*	66.5
InSeIn w/ OCRNet (ours)	HRNetV2-W48	46.8*	82.9*	67.6
SegFormer [44]	MiT-B4	50.3	82.2	67.1
InSeIn w/ SegFormer (ours)	MiT-B4	51.0	82.7	69.2
Mask2Former [9]	Swin-L	56.1	83.5*	77.2
InSeIn w/ Mask2Former (ours)	Swin-L	56.7	84.0*	77.8
OneFormer [25]	ConvNeXt-XL	57.4	83.8	78.0
InSeIn w/ OneFormer (ours)	ConvNeXt-XL	58.0	84.3	78.9
SegMAN [15]	SegMAN-B	52.6	83.6	77.5
InSeIn w/ SegMAN (ours)	SegMAN-B	53.7	84.4	78.3

Table 2. Comparison to Beyond Pixels [22] on the Cityscapes test set using two baselines, SegFormer and Mask2Former. Beyond Pixels is also fully supervised, as InSeIn.

Method	mIoU (%)
Beyond Pixels w/ SegFormer	82.5
InSeIn w/ SegFormer (ours)	82.7
Beyond Pixels w/ Mask2Former	83.7
InSeIn w/ Mask2Former (ours)	84.0

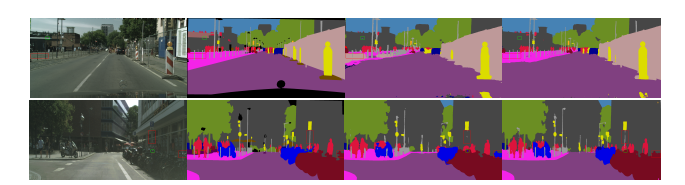


Figure 4. Qualitative comparison on Cityscapes. Best viewed on a screen with full zoom. From left to right: input image, ground-truth semantic labels, prediction of Mask2Former [9] network and InSeIn.

applied offline in each iteration to reduce the memory footprint. We report semantic segmentation performance using mean Intersection over Union (mIoU). The value of α is fixed to 10^{-9} for all examined datasets after a search in log-space in the interval $\left[10^{-10},10^{-5}\right]$ based on validation performance.

Training setup. For all networks on which we implement InSeIn, we have used a batch size of 4 for Cityscapes and ACDC and 8 for ADE20K. The training protocol and hyperparameters remain the same as those for the base networks on each respective dataset. For ACDC, we applied the same setup as the corresponding baselines applied on the Cityscapes dataset. We used mmsegmentation [10] to implement InSeIn on the baseline network SegFormer-B4 [44].

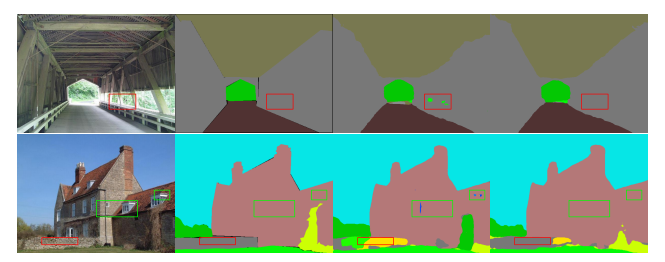


Figure 5. Qualitative comparison on ADE20K. Best viewed on a screen with full zoom. From left to right: input image, ground-truth semantic labels, and predictions of OCRNet [48] and InSeIn.

4.3. Comparison to The State of The Art

Tab. 1 compares InSeIn with a wide range of state-of-theart methods for semantic segmentation on Cityscapes [11], ADE20K [52], and ACDC [36]. Overall, InSeIn achieves significant improvements in mIoU across all five network architectures on which we have implemented it and across all three datasets. On Cityscapes, we observe a consistent 0.5-0.8% improvement in mIoU with InSeIn on all architectures. On ADE20K, InSeIn achieves 1.2% improvement over the baseline OCRNet [48] and 0.7% over the baseline SegFormer-B4. On ACDC, InSeIn achieves 1.1% improvement over the baseline OCRNet and 2.1% over the baseline SegFormer-B4. Overall, improvements with InSeIn are consistent across all examined network architectures. This evidence shows that InSeIn can improve the segmentation performance of a general baseline network on which it is applied.

Tab. 2 presents a comparison of InSeIn with a recent competing plug-and-play model, Beyond Pixels [22], on the Cityscapes dataset, implemented on two of our examined baseline networks, namely SegFormer and Mask2Former, for fully supervised segmentation. InSeIn consistently outperforms Beyond Pixels. Tab. 3 shows the class-wise comparison of IoU on the Cityscapes validation set for InSeIn and the corresponding baselines. We observe that InSeIn achieves a consistent improvement in IoU scores across most of the 19 classes. InSeIn with OCRNet [48], Seg-MAN [15], and SegFormer [44] show improvement in small challenging classes of the Cityscapes dataset. While we can observe an all-around and consistent improvement with Mask2Former [9] and OneFormer [25]. Tab. 4 shows the class-wise comparison of IoU on the ACDC test set for InSeIn and the corresponding baselines. We also observe that InSeIn achieves an overall improvement in IoU scores across the classes, especially over the SegFormer baseline. InSeIn achieves significant gains across all baselines for challenging small-instance classes such as motorcycle, bicycle, and rider.

Qualitative results on Cityscapes. In Fig. 4, in the first row, baseline prediction, a building segment infeasibly in-

Table 3. Comparison of class-level IoU of OCRNet, SegFormer, Mask2Former, OneFormer, and SegMAN to their InSeIn-upgraded versions on the Cityscapes validation set. Training and evaluation are performed using the complete training and validation sets, respectively.

Method	road	sidew.	build.	wall	fence	pole	light	sign	veget.	terrain	sky	person	rider	car	truck	snq	train	motorc.	bicycle	mIoU
OCRNet [48] Ours			93.1 93.4		63.6 64.2													~		80.3 81.3
SegFormer [44] Ours			93.7 93.8		65.4 72.3				,											82.0 83.6
Mask2Former [9] Ours			94.0 94.8																81.5 83.3	83.3 85.3
OneFormer [25] Ours			94.8 94.9		67.2 69.1										81.4 81.6					84.6 85.3
SegMAN [15] Ours			94.3 94.3																	83.8 84.5

Table 4. Comparison of class-level IoU of OCRNet, SegFormer, Mask2Former, OneFormer, and SegMAN to their InSeIn-upgraded versions on the ACDC test set. Training and evaluation are performed using the complete training and test sets, respectively.

Method	road	sidew.	build.	wall	fence	pole	light	sign	veget.	terrain	sky	person	rider	car	truck	snq	train	motorc.	bicycle	mIoU
OCRNet [48]	93.4	77.2	87.1	50.0	45.2	48.6	60.4	61.3	85.4	59.4	95.5	58.5	40.5	87.4	63.6	76.3	80.6	41.6	53.2	66.5
Ours	92.5	71.6	87.2	45.3	39.9	54.2	70.2	68.2	86.4	50.8	94.8	65.2	45.5	87.2	60.9	69.9	84.5	50.6	59.9	67.6
SegFormer [44]	94.6	78.3	88.4	51.6	47.4	48.0	62.1	61.2	87.0	66.8	95.6	59.8	39.0	87.0	63.1	73.8	79.1	38.4	52.7	67.1
Ours	94.8	79.5	88.5	54.2	50.4	48.7	63.7	64.2	87.9	66.2	95.9	61.2	42.0	88.2	70.8	77.9	84.1	42.3	54.6	69.2
Mask2Former [9]	96.5	84.7	93.2	64.7	59.5	72.0	80.6	78.9	91.1	72.1	96.7	77.7	44.4	91.6	75.9	71.0	92.4	58.5	65.9	77.2
Ours	96.4	84.3	92.9	65.7	61.2	66.7	78.7	79.5	91.0	71.9	97.0	77.5	56.6	91.3	76.9	73.3	91.6	58.9	67.0	77.8
OneFormer [25]	94.5	80.9	91.9	66.8	57.7	64.3	74.9	75.0	79.2	68.7	87.7	78.0	62.1	92.9	84.9	91.5	94.0	68.7	68.4	78.0
Ours	98.7	86.9	93.3	58.8	60.3	65.7	73.0	78.3	93.5	72.8	95.6	85.9	71.2	95.9	73.3	82.3	69.5	67.2	75.9	78.8
SegMAN [15]	94.5	78.2	92.0	61.9	55.0	64.8	73.7	72.6	88.3	67.3	95.3	77.1	60.2	92.6	84.0	86.8	92.4	67.5	68.6	77.5
Ours	94.6	80.7	92.1	69.5	57.9	64.5	75.2	75.4	79.2	68.5	87.9	78.6	62.3	92.7	84.8	91.6	94.0	68.8	68.5	78.3

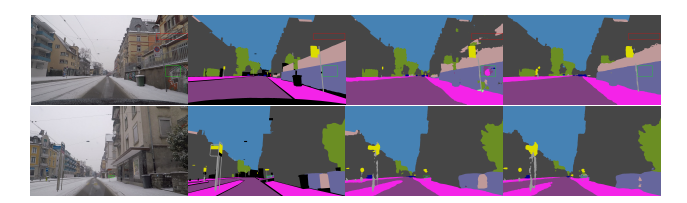


Figure 6. Qualitative comparison on ACDC. Best viewed on a screen at full zoom. From left to right: input image, ground-truth semantic labels, and predictions of SegFormer [44] network and InSeIn.

cludes a sky segment marked with *green* boxes, InSeIn rectifies it and also better segments the sidewalk marked with *red* boxes. The second row, baseline prediction, a bicycle infeasibly includes a motorcycle segment marked with *green* boxes on the right of the image. InSeIn rectifies this erroneous motorcycle segment.

Qualitative results on ADE20K. In Fig. 5, in the first row, baseline prediction, the bridge segment includes a vegeta-

tion segment marked with *red* boxes, while InSeIn successfully rectifies such erroneous prediction. The second row, baseline prediction, building segment infeasibly includes a segment of the sea marked with *green* boxes. InSeIn rectifies it completely, and the *red* bounding boxes show additional parts of the prediction which are improved by InSeIn. **Qualitative results on ACDC.** In Fig. 6, in the first row, baseline prediction, wall segment infeasibly includes a sidewalk segment marked with *green* boxes. InSeIn successfully rectifies the infeasibility. The second row, baseline prediction, building segment infeasibly includes a wall segment marked with *green* boxes. InSeIn successfully predicts a wall label on that region. In both examples, *red* boxes highlight miscellaneous parts of the predictions where InSeIn improves upon baseline.

4.4. Evaluation of Prediction Feasibility

Here we demonstrate the efficacy of our model. The complete per-dataset counts of the feasible and infeasible inclu-

Table 5. Feasible and infeasible inclusion pair statistics for different datasets. The statistics are computed on the training set of each dataset. Infeasible pair counts exclude pairs that do not co-occur in any image of the dataset.

Dataset \ Type of class pair	Feasible	Infeasible
Cityscapes (19 classes)	162	180
ADE20K (150 classes)	11070	11280
ACDC (19 classes)	118	224

Table 6. Comparison of prediction feasibility with state-of-theart models on Cityscapes and ACDC. Results are reported with our mINF metric (%, lower is better) on the Cityscapes and ACDC test sets

Method \ Dataset	Cityscapes	ACDC
SegFormer [44]	4.0	8.0
InSeIn w/ SegFormer (ours)	0.1	0.2
Mask2Former [9]	3.2	7.3
InSeIn w/ Mask2Former (ours)	0.1	0.1
OneFormer [25]	3.0	7.1
InSeIn w/ OneFormer (ours)	0.1	0.1

Table 7. False response error (%, lower is better) on the Cityscapes and ACDC validation sets. We have set boundary regions to 15 pixels.

-8		
Method \ Dataset	Cityscapes	ACDC
SegFormer [44]	23.7	37.6
InSeIn w/ SegFormer (ours)	22.2	35.9
Mask2Former [9]	22.0	29.3
InSeIn w/ Mask2Former (ours)	20.8	28.0
OneFormer [25]	21.7	28.3
InSeIn w/ OneFormer (ours)	19.9	26.8

sion pairs are reported in Tab. 5. Algorithm 1 is applied to the training set of every dataset, even when we train the networks on the union of the training and validation sets.

We define a class-level metric to measure how well predictions conform to our inclusion constraint, which we term mean infeasibility normalized frequency (mINF), as

$$mINF = \frac{1}{|\mathcal{C}'|} \sum_{(c_i, c_j) \in \mathcal{C}'} \frac{f_{inclusion}(c_i, c_j)}{f_{co\text{-}occur}(c_i, c_j)}.$$
 (6)

We compute $f_{\text{co-occur}}(c_i,c_j)$, i.e., the frequency of co-occurrence of the classes in the infeasible class pair (c_i,c_j) in the set of predicted labelings on the evaluation set. $f_{\text{inclusion}}(c_i,c_j)$ is the frequency of the occurrence of infeasible inclusions for class pair (c_i,c_j) in the set of predicted labelings on the evaluation set. An mINF of 0 signifies the complete absence of infeasible inclusions in the predicted labelings. We report mINF scores in Tab. 6 for SegFormer, Mask2Former, and OneFormer models on Cityscapes and

Table 8. Ablation study of InSeIn with Mask2Former-SwinB on the Cityscapes validation set. Number of iterations used for max-pooling kernels 5×5 and 7×7 is 60k.

Kernel-size	Stride	Padding	T	mIoU
3×3	1	1	128	85.3
5×5	1	2	60	81.8
7×7	1	3	3	79.8

ACDC. These results show that InSeIn can almost fully adhere to the inclusion constraint imposed by our inclusion loss.

We have also computed another pixel-level metric, namely the false response error [3, 51], with results for three representative network architectures shown in Tab. 7. Lower values imply that the prediction feature maps contain less erroneous pixels. We observe a significant improvement with InSeIn over the baseline predictions across all three examined architectures.

We additionally conduct an "oracle" experiment, by manually filtering with a conceptual process the original set of infeasible class pairs extracted from Cityscapes, which contains 180 pairs. After this filtering, the number of infeasible pairs becomes 120. The mIoU on the Cityscapes test set of the InSeIn model trained with this updated set of infeasible pairs based on a Mask2Former architecture is 83.9%, which is on a par with the original score presented in Tab. 1. This confirms that our data-driven constraint extraction already provides a meaningful set of constraints for moderate-size datasets such as Cityscapes, with minimal to no impact from potential spurious infeasibility constraints that are included to our loss due to the rare occurrence of the respective configurations in practice.

4.5. Ablation Study

Tab. 8 ablates InSeIn on Cityscapes using Mask2Former as the baseline. We report validation set performance. We adjust the padding appropriately to preserve spatial dimensions across dilation iterations. We observe that by increasing the kernel size with a decrease in the number of iterations for max-pooling, performance tends to decrease. The reason behind this decrease is that a bigger structuring element, i.e., the max-pooling kernel, enables the propagation of the border pixels to the interior portion of the feature map, which should otherwise be disconnected, and as a result, the infeasible included segment is not opened correctly. Thus, inclusion loss will assume too high a value, penalizing feasible segments.

5. Conclusion and Future Work

In this paper, rather than building a new semantic segmentation architecture, we have attempted to enhance any existing state-of-the-art network by enforcing a data-driven

high-level constraint into the network. Our method, InSeIn, constitutes a light-weight, plug-and-play module for semantic segmentation, which can be coupled with any network architecture to improve accuracy and conformity to our exemplary inclusion prior. Overall, InSeIn successfully attains our goal of structural feasibility in segmentation, both in the qualitative and quantitative sense.

References

- [1] Stamatis Alexandropoulos, Christos Sakaridis, and Petros Maragos. OVeNet: Offset vector network for semantic segmentation. In *Proceedings of the IEEE/CVF Winter Conference on Applications of Computer Vision (WACV)*, 2024. 2
- [2] Davide Antonutti, Axel de Nardin, Silvia Zottin, Claudio Piciarelli, and Gian Luca Foresti. Multi-modal analysis of biparametric mri slices for lesion detection in prostate cancer screening. *IEEE Access*, 2025. 3
- [3] Linwei Chen, Lin Gu, and Ying Fu. When semantic segmentation meets frequency aliasing. In *International Conference on Learning Representations*, 2024. 8
- [4] Lei Chen, Yang Wang, Jibin Yang, Yunfei Zheng, Tong Han, Bo Zhang, and Tieyong Cao. Uncertainty-aware focal loss for object segmentation. *Engineering Applications of Artifi*cial Intelligence, 2025. 2
- [5] Liang-Chieh Chen, Yi Yang, Jiang Wang, Wei Xu, and Alan L Yuille. Attention to scale: Scale-aware semantic image segmentation. In *CVPR*, 2016. 1
- [6] Liang-Chieh Chen, George Papandreou, Iasonas Kokkinos, Kevin Murphy, and Alan L. Yuille. Deeplab: Semantic image segmentation with deep convolutional nets, atrous convolution, and fully connected crfs. *IEEE Transactions on Pattern Analysis and Machine Intelligence*, 40(4):834–848, 2018. 6
- [7] Liang-Chieh Chen, Yukun Zhu, George Papandreou, Florian Schroff, and Hartwig Adam. Encoder-decoder with atrous separable convolution for semantic image segmentation. In *Proceedings of the European conference on computer vision* (ECCV), pages 801–818, 2018. 1
- [8] Liang-Chieh Chen, Yukun Zhu, George Papandreou, Florian Schroff, and Hartwig Adam. Encoder-decoder with atrous separable convolution for semantic image segmentation. In ECCV, 2018. 6
- [9] Bowen Cheng, Ishan Misra, Alexander G. Schwing, Alexander Kirillov, and Rohit Girdhar. Masked-attention mask transformer for universal image segmentation. In 2022 IEEE/CVF Conference on Computer Vision and Pattern Recognition (CVPR), pages 1280–1289, 2022. 1, 2, 6, 7, 8
- [10] MMSegmentation Contributors. MMSegmentation:
 Openmmlab semantic segmentation toolbox and benchmark. https://github.com/open-mmlab/mmsegmentation, 2020. 6
- [11] Marius Cordts, Mohamed Omran, Sebastian Ramos, Timo Rehfeld, Markus Enzweiler, Rodrigo Benenson, Uwe Franke, Stefan Roth, and Bernt Schiele. The cityscapes

- dataset for semantic urban scene understanding. In *Proceedings of the IEEE Conference on Computer Vision and Pattern Recognition (CVPR)*, 2016. 2, 4, 5, 6
- [12] Xueqing Deng, Peng Wang, Xiaochen Lian, and Shawn Newsam. Nightlab: A dual-level architecture with hardness detection for segmentation at night. In 2022 IEEE/CVF Conference on Computer Vision and Pattern Recognition (CVPR), 2022. 2
- [13] Henghui Ding, Xudong Jiang, Ai Qun Liu, Nadia Magnenat Thalmann, and Gang Wang. Boundary-aware feature propagation for scene segmentation. In 2019 IEEE/CVF International Conference on Computer Vision (ICCV), 2019. 2
- [14] Alexey Dosovitskiy. An image is worth 16x16 words: Transformers for image recognition at scale. arXiv preprint arXiv:2010.11929, 2020. 1
- [15] Yunxiang Fu, Meng Lou, and Yizhou Yu. Segman: Omniscale context modeling with state space models and local attention for semantic segmentation. In *IEEE/CVF Conference on Computer Vision and Pattern Recognition*, 2025. 2, 6, 7
- [16] Rafael Gonzalez and Richard Woods. Digital Image Processing. Pearson Deutschland, 2017. 2
- [17] A.K. Griffith. Edge detection in simple scenes using a priori information. *IEEE Transactions on Computers*, 1973.
- [18] Arnold K. Griffith. Mathematical models for automatic line detection. J. ACM, 1973. 2
- [19] Zhangxuan Gu, Li Niu, Haohua Zhao, and Liqing Zhang. Hard pixel mining for depth privileged semantic segmentation. *IEEE Transactions on Multimedia*, 2021. 2
- [20] Meng-Hao Guo, Cheng-Ze Lu, Qibin Hou, Zhengning Liu, Ming-Ming Cheng, and Shi-Min Hu. SegNeXt: Rethinking convolutional attention design for semantic segmentation. In Advances in Neural Information Processing Systems (NeurIPS), 2022. 1
- [21] Kaiming He, Xiangyu Zhang, Shaoqing Ren, and Jian Sun. Deep residual learning for image recognition. In *Proceedings of the IEEE conference on computer vision and pattern recognition*, pages 770–778, 2016. 1
- [22] Prantik Howlader, Srijan Das, Hieu Le, and Dimitris Samaras. Beyond pixels: Semi-supervised semantic segmentation with multi-scale patch-based multi-label classifier. In Computer Vision ECCV 2024: 18th European Conference, Milan, Italy, September 29–October 4, 2024, Proceedings, Part LXXV, 2024. 6
- [23] Heng Huang, Jia Chen, Tao Chen, Jun Li, and Antonio Plaza. Hybrid tunnel entrance detection via multiple morphological component-based texture enhancement. *IEEE Journal of Selected Topics in Applied Earth Observations and Remote Sensing*, 2025. 3
- [24] Muhammad Hannan Hunafa, M Luthfi Ramadhan Mgs, Alif Wicaksana Ramadhan, Muhammad Febrian Rachmadi, and Wisnu Jatmiko. Weighted ensemble based on prisoner dilemma for facial expression recognition. *IEEE Access*, 2025. 3
- [25] Jitesh Jain, Jiachen Li, MangTik Chiu, Ali Hassani, Nikita Orlov, and Humphrey Shi. OneFormer: One Transformer to Rule Universal Image Segmentation. In *IEEE/CVF Conference on Computer Vision and Pattern Recognition*, 2023. 2, 6, 7, 8

- [26] Tsung-Wei Ke, Jyh-Jing Hwang, Ziwei Liu, and Stella X. Yu. Adaptive affinity fields for semantic segmentation. In Computer Vision ECCV 2018: 15th European Conference, Munich, Germany, September 8-14, 2018, Proceedings, Part I, page 605–621, Berlin, Heidelberg, 2018. Springer-Verlag.
- [27] Xiaoxiao Li, Ziwei Liu, Ping Luo, Chen Change Loy, and Xiaoou Tang. Not all pixels are equal: Difficulty-aware semantic segmentation via deep layer cascade. In 2017 IEEE Conference on Computer Vision and Pattern Recognition (CVPR), 2017. 2
- [28] Tsung-Yi Lin, Priya Goyal, Ross Girshick, Kaiming He, and Piotr Dollár. Focal loss for dense object detection. *IEEE Transactions on Pattern Analysis and Machine Intelligence*, 2020. 3
- [29] Ze Liu, Yutong Lin, Yue Cao, Han Hu, Yixuan Wei, Zheng Zhang, Stephen Lin, and Baining Guo. Swin Transformer: Hierarchical Vision Transformer using Shifted Windows. In 2021 IEEE/CVF International Conference on Computer Vision (ICCV), pages 9992–10002, Los Alamitos, CA, USA, 2021. IEEE Computer Society. 1
- [30] Jonathan Long, Evan Shelhamer, and Trevor Darrell. Fully convolutional networks for semantic segmentation. In 2015 IEEE Conference on Computer Vision and Pattern Recognition (CVPR), pages 3431–3440, Los Alamitos, CA, USA, 2015. IEEE Computer Society. 1
- [31] C. Lopez-Molina, B. De Baets, and H. Bustince. Quantitative error measures for edge detection. *Pattern Recognition*, pages 1125–1139, 2013. 2
- [32] Alberto Martelli. Edge detection using heuristic search methods. *Computer Graphics and Image Processing*, 1972. 2
- [33] Jing Nie, Yanwei Pang, Jin Xie, Jungong Han, and Xuelong Li. Binocular image dehazing via a plain network without disparity estimation. *IEEE Transactions on Multimedia*, 2024. 2
- [34] George Papandreou, Liang-Chieh Chen, Kevin Murphy, and Alan L Yuille. Weakly- and semi-supervised learning of a dcnn for semantic image segmentation. In *ICCV*, 2015. 1
- [35] Giuseppe Papari and Nicolai Petkov. Edge and line oriented contour detection: State of the art. *Image and Vision Computing*, 2011. 2
- [36] Christos Sakaridis, Dengxin Dai, and Luc Van Gool. ACDC: The Adverse Conditions Dataset with Correspondences for semantic driving scene understanding. In *Proceedings of* the IEEE/CVF International Conference on Computer Vision (ICCV), 2021. 2, 5, 6
- [37] Karen Simonyan and Andrew Zisserman. Very deep convolutional networks for large-scale image recognition. In *International Conference on Learning Representations*, 2015.
- [38] Juan Miguel Valverde and Jussi Tohka. Region-wise loss for biomedical image segmentation. *Pattern Recognition*, 136: 109208, 2023. 3
- [39] Lucas J van Vliet, Ian T Young, and Guus L Beckers. A nonlinear laplace operator as edge detector in noisy images. *Computer Vision, Graphics, and Image Processing*, 1989. 2

- [40] Haochen Wang, Junsong Fan, Yuxi Wang, Kaiyou Song, Tiancai Wang, Xiangyu Zhang, and Zhaoxiang Zhang. Bootstrap masked visual modeling via hard patch mining. IEEE Transactions on Pattern Analysis and Machine Intelligence, 2025. 3
- [41] Jingdong Wang, Ke Sun, Tianheng Cheng, Borui Jiang, Chaorui Deng, Yang Zhao, Dong Liu, Yadong Mu, Mingkui Tan, Xinggang Wang, Wenyu Liu, and Bin Xiao. Deep high-resolution representation learning for visual recognition. TPAMI, 2019. 1, 6
- [42] Wenhai Wang, Enze Xie, Xiang Li, Deng-Ping Fan, Kaitao Song, Ding Liang, Tong Lu, Ping Luo, and Ling Shao. Pyramid vision transformer: A versatile backbone for dense prediction without convolutions. In 2021 IEEE/CVF International Conference on Computer Vision (ICCV), pages 548–558, 2021.
- [43] Longsheng Wei and Yuhang Liao. Lnformer: Lightweight design for nighttime semantic segmentation with transformer. IEEE Transactions on Instrumentation and Measurement, 2025. 2
- [44] Enze Xie, Wenhai Wang, Zhiding Yu, Anima Anandkumar, Jose M Alvarez, and Ping Luo. SegFormer: Simple and efficient design for semantic segmentation with transformers. In *Advances in Neural Information Processing Systems* (NeurIPS), 2021. 2, 4, 6, 7, 8
- [45] Lijun Yin, Anup Basu, and Ja Kwei Chang. Scalable edge enhancement with automatic optimization for digital radiographic images. *Pattern Recognition*, 2004. 2
- [46] Zuobin Ying, Zhengcheng Lin, Zhenyu Li, Xiaochun Huang, and Weiping Ding. Scdf: Seeing clearly through dark and fog, an adaptive semantic segmentation scheme for autonomous vehicle. *IEEE Transactions on Intelligent Transportation Systems*, 2025. 2
- [47] Fisher Yu and Vladlen Koltun. Multi-scale context aggregation by dilated convolutions. In *International Conference on Learning Representations*, 2016. 1
- [48] Yuhui Yuan, Xilin Chen, and Jingdong Wang. Object-contextual representations for semantic segmentation. In ECCV, 2020. 1, 2, 6, 7
- [49] Hang Zhang, Chongruo Wu, Zhongyue Zhang, Yi Zhu, Haibin Lin, Zhi Zhang, Yue Sun, Tong He, Jonas Mueller, R Manmatha, et al. Resnest: Split-attention networks. In Proceedings of the IEEE/CVF conference on computer vision and pattern recognition, pages 2736–2746, 2022. 1
- [50] Hengshuang Zhao, Jianping Shi, Xiaojuan Qi, Xiaogang Wang, and Jiaya Jia. Pyramid Scene Parsing Network. In IEEE Conference on Computer Vision and Pattern Recognition (CVPR), 2017. 1, 6
- [51] Weiguang Zhao, Rui Zhang, Qiufeng Wang, Guangliang Cheng, and Kaizhu Huang. Bfanet: Revisiting 3d semantic segmentation with boundary feature analysis. In *Proceedings* of the Computer Vision and Pattern Recognition Conference (CVPR), pages 29395–29405, 2025. 8
- [52] Bolei Zhou, Hang Zhao, Xavier Puig, Tete Xiao, Sanja Fidler, Adela Barriuso, and Antonio Torralba. Semantic understanding of scenes through the ADE20K dataset. *International Journal of Computer Vision*, 127:302–321, 2019. 2, 5, 6